# 4

# Numerical Investigation of Plasma Flows Inside Segmented Constrictor Type Arc-Heater

Kyu-Hong Kim
*School of Mechanical and Aerospace Engineering, Seoul National University*
*Korea*

## 1. Introduction

Arc-jet wind tunnels produce the flow conditions as an entry vehicle entering the atmosphere of a planet. They are widely used in experimental investigations of heat shield materials and thermal protection systems (TPSs). For a detailed analysis of experimental data, it is very important to know the conditions of the plasma flow that reaches a specimen of heat shield material or the TPS; e.g., the total pressure, total temperature and turbulence intensity of the plasma flow. However, it is hard to measure the properties of plasma flow because of its high temperature. In particular, it is almost impossible to measure the turbulence intensity inside an arc heater. On the other hand, if accurate physical models are adopted, computational fluid dynamics (CFD) can provide very useful information on plasma flow, and play an important role on the analysis of experimental data.

Several types of arc heaters have been developed according to the required range of total pressure and total enthalpy; these include the Huels type, constricted type, segmented constrictor type, inductively-coupled plasma (ICP), MPD (magnetoplasmadynamic) and so on. Among them, the segmented type and the Huels-type arc heaters have been widely used in aerospace applications since they can provide a large amount of plasma flow at a high total pressure condition. Compared to other types of arc heaters, the Huels arc heater produces a severe arc fluctuation phenomenon in time and space whereas a segmented arc heater produces stable arc flow throughout a long constrictor. At present, CFD analysis is more useful for the analysis of segmented type arc heaters since it is not easy to calculate a Huels-type arc heater accurately, even though state-of-the-art CFD technologies have been applied.

There have been several numerical investigations of the flow inside segmented arc heaters; these studies mainly focused on the improvement of physical models including radiation and the turbulence model. In the 1970s, Nicolet et al. (1975), based on the work of Watson and Pegot (1967), developed the ARCFLO numerical code. The ARCFLO code adopted a two-band radiation model and an algebraic turbulence model. However, since ARCFLO uses the space marching technique, it requires knowledge of downstream conditions in advance. Thus, the applicability of the ARCFLO code was quite restrictive in the actual design of arc heaters. Therefore, Kim et al. (2000) developed a time-marching code, ARCFLO2, to overcome this shortcoming. ARCFLO2 retained the two-band radiation model and the algebraic turbulence model. Sakai and Olejniczak (2001, 2003) improved the numerical models of ARCFLO and ARCFLO2 by adopting a new three-

band radiation model that was quite consistent with detailed line-by-line calculation; this code was named ARCFLO3. However, ARCFLO2 and ARCFLO3 could not always provide acceptable accuracy for a wide range of arc heaters since it could not predict turbulence physics accurately. Recently, Lee et al. (2007) improved ARCFLO3 and named their revised code ARCFLO4. The ARCFLO4 code adopted a two-equation turbulence model instead of an algebraic turbulence model while retaining the three-band radiation model of ARCFLO3. ARCFLO4 adopted k-ε (Jones & Launder, 1972), k-ω (Wilcox, 1998), and kω-SST model (Menter, 1994) which are able to express convective physics of turbulence and do not explicitly require a mixing length. Subsequently, ARCFLO4 was improved to handle an air–argon mixture as a working gas, and its numerical accuracy was sufficiently enhanced to be used as an arc heater design tool (Lee et al., 2008). Recently, ARCFLO4 was improved again to solve electronic field and magnetohydrodynamic (MHD) equations.

This chapter is focused on two issues. First, the accuracy level of recent CFD technology for arc-heated plasma flow is introduced and validated. As previously mentioned, arc heaters are widely used for high enthalpy flow experiments, and the values of total pressure, total enthalpy, and turbulence intensity at the surface of the specimen are important for a detailed analysis of experimental data. For example, in ablation experiments, the turbulent intensity of plasma flow may accelerate an ablation several-fold compared to laminar plasma flow. In order to validate the ARCFLO4 code, I first describe the results of the CFD analysis by comparison with real experimental data. Second, the potential use of the computational code as a design tool for arc heater is discussed. The empirical design process is possible if an established database exists based on the extensive experience of designers. However, if this is not the case, it is hard to determine the required total enthalpy, the amount of the heat flux that should be removed by cooling process, and so on. On the other hand, the required database can be obtained easily by CFD analysis if an accurate calculation of arc-heated flow is possible. Thus, in this chapter, I consider the performance variation of an arc heater according to changes in design variables in order to assess the use of ARCFLO4 as a design tool for arc heaters.

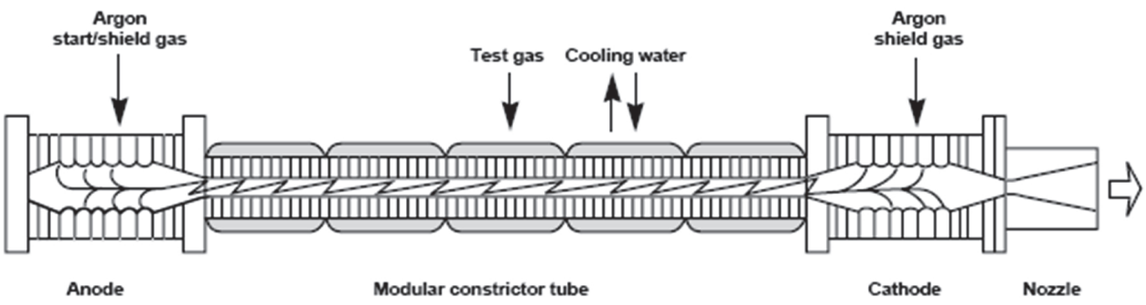


Fig. 1. Schematic Drawing of a Segmented Arc Heater

The contents of the remainder of this chapter are as follows. The governing equation and the physical modeling are explained in Section 2. In Section 3, validations and a flow analysis of the arc heater flow are described. Finally, Section 4 describes a parametric study process to examine the possibility of using a CFD code as an arc heater design tool.

## 2. Governing equations and physical modeling

### 2.1 Governing equations

The governing equations are hyperbolic 2-D axisymmetric Navier-Stokes equations that include Joule heating by arc, radiation, the swirling effect, and turbulence phenomena. The governing equations are as follows:

$$\frac{\partial \mathbf{Q}}{\partial t}+\frac{\partial \mathbf{E}}{\partial x}+\frac{\partial \mathbf{F}}{\partial y}+\mathbf{H}=\frac{\partial \mathbf{E_v}}{\partial x}+\frac{\partial \mathbf{F_v}}{\partial y}+\mathbf{H_v}+\mathbf{I} \tag{1}$$

where

$$\mathbf{Q}=\begin{bmatrix}\rho\\ \rho_{Ar}\\ \rho u\\ \rho v\\ \rho w\\ \rho E\end{bmatrix},\ \mathbf{E}=\begin{bmatrix}\rho u\\ \rho_{Ar}u\\ \rho uu+p\\ \rho uv\\ \rho uw\\ \rho uH\end{bmatrix},\ \mathbf{F}=\begin{bmatrix}\rho v\\ \rho_{Ar}v\\ \rho uv\\ \rho vv+p\\ \rho vw\\ \rho vH\end{bmatrix},\ \mathbf{H}=\frac{1}{y}\begin{bmatrix}\rho v\\ \rho_{Ar}v\\ \rho uv\\ \rho vv-\rho ww\\ 2\rho vw\\ \rho vH\end{bmatrix},$$

$$\mathbf{E_v}=\begin{bmatrix}0\\ \rho D_{Ar}\dfrac{\partial c_{Ar}}{\partial x}\\ \tau_{xx}\\ \tau_{xy}\\ \tau_{x\theta}\\ u\tau_{xx}+v\tau_{xy}+w\tau_{x\theta}-q_{c,x}-q_{R,x}\end{bmatrix},\ \mathbf{F_v}=\begin{bmatrix}0\\ \rho D_{Ar}\dfrac{\partial c_{Ar}}{\partial y}\\ \tau_{xy}\\ \tau_{yy}\\ \tau_{y\theta}\\ u\tau_{xy}+v\tau_{yy}+w\tau_{y\theta}-q_{c,y}-q_{R,y}\end{bmatrix},$$

$$\mathbf{H_v}=\frac{1}{y}\begin{bmatrix}0\\ \rho D_{Ar}\dfrac{\partial c_{Ar}}{\partial y}\\ \tau_{xy}\\ \tau_{yy}-\tau_{\theta\theta}\\ 2\tau_{y\theta}\\ u\tau_{xy}+v\tau_{yy}+w\tau_{y\theta}-q_{c,y}-q_{R,y}\end{bmatrix},\ \mathbf{I}=\begin{bmatrix}0\\ 0\\ 0\\ 0\\ 0\\ -j\cdot E\end{bmatrix}. \tag{2}$$

In practical applications, argon and air are injected separately in a segmented arc heater (Terrazas-Salinas & Cornelison, 1999). Thus, the continuity equation for argon gas is also solved. The thermodynamic and transport properties of the mixture, including Ar and Ar+, are calculated in a thermal equilibrium state. I is the Joule heating term and $q_R$ is the radiant flux. As shown in Eq. 2, swirl velocity w is considered in the momentum equation and the energy equation to reflect the effects of swirl injection. Numerically, the governing equations are then discretized using the finite volume method. The AUSMPW+ scheme

(Kim et al., 2001) is used for the spatial discretization of the inviscid flux. A central difference scheme is used for the calculation of the viscous flux. For time integration, LU-SGS (Jameson & Yoon, 1987) method is used and the spatial accuracy is improved by MLP(Kim & Kim, 2005).

### 2.2 Physical modeling

#### 2.2.1 Equilibrium composition, thermodynamic properties and transport properties

In this chapter, the working gas is assumed to be in a chemical equilibrium state. Chemical equilibrium is described by minimization of the Gibbs free energy formulation. The equilibrium composition is obtained with 11-species ($N_2$, $O_2$, Ar, N, O, NO, Ar+, N+, O+, NO+ and e-). Thermodynamic data of each species are from the NASA Glenn thermodynamic database (Mcbride et al., 2002) which is known to be valid for temperatures up to 20,000 K. Transport properties are computed using the approximate formulations of Gupta et al. (1990) and Yos (1963). The collision cross sections (πΩij(1,1), πΩij(2,2)) including the air species are obtained from Park (2001) and Kim et al. (2006). However, for the ionized species, the effective Coulomb cross section of Gupta et al. (1990) and Yos (1963) is used. To solve the continuity equation for the argon gas, the effective binary diffusion coefficient is required. Thus,

$$D_{im} = \frac{1 - n_i}{\sum_{j=1, j\neq i}^{N_S} n_j / D_{ij}} \tag{3}$$

where $D_{ij}$ is an ordinary binary diffusion coefficient and can be computed as follows:

$$D_{ij} = \frac{kT}{p\Delta_{ij}^{(1)}}, \tag{4}$$

with

$$\Delta_{ij}^{(1)} = \frac{8}{3}\left[\frac{2M_iM_j}{\pi RT\left(M_i + M_j\right)}\right]^{1/2} \pi\Omega_{ij}^{(1,1)} \tag{5}$$

In this computation, the continuity equation for argon gas does not distinguish between neutral argon and ionized argon. Thus, the diffusion coefficient for argon gas is finally calculated as follows (the details are introduced in Lee et al. (2008)):

$$D_{Ar} = \frac{D_{Arm}c_{Ar} + D_{Ar^+m}c_{Ar^+}}{c_{Ar} + c_{Ar^+}} \tag{7}$$

#### 2.2.2 Turbulence model

Turbulence is known to play an important role in the flow physics of an arc heater. In numerical calculations, algebraic turbulence models have been used wherein the turbulent fluctuating quantities are correlated to the mean flow quantities using algebraic relations. However, such calculations do not reflect the convection effect of turbulence since the local

rate of turbulence production is equal to that of turbulence dissipation. In addition, the algebraic model needs the turbulence mixing length in order to provide an accurate numerical result. To overcome this shortcoming, more advanced turbulence models that possess less empirical turbulence coefficients are introduced for arc-heated flow (Lee et al. 2007). In this chapter, I introduce three two-equation turbulence models: the k–ε model of Jones and Launder (1972), the k–ω model of Wilcox (1998), and the k–ω SST model of Menter (1994).

#### 2.2.2.1 *k*-ε two-equation model (Jones & Launder, 1972)

The k-ε model is the most widely known and extensively used two-equation eddy viscosity model. The main references for this model are described by Jones and Launder (1972). The model gives reasonably good results for free-shear-layer flows with relatively small pressure gradients. The Reynolds stresses are modeled as follows:

$$\tau_{tij} = 2\mu_t\left(s_{ij} - s_{nn}\delta_{ij}/3\right) - 2\rho k\delta_{ij}/3\,, \tag{6}$$

where $\mu_t$ is the eddy viscosity, $s_{ij}$ is the mean-velocity strain-rate tensor, ρ is the fluid density, k is the turbulent kinetic energy, and $\delta_{ij}$ is the Kronecker delta. The eddy viscosity is defined as a function of the turbulent kinetic energy, k, and the turbulent dissipation rate, ε.

$$\mu_t = c_\mu f_\mu \rho k^2/\varepsilon\,. \tag{7}$$

The model coefficient, $c_\mu$, is determined by equilibrium analysis at high Reynolds numbers, and the damping function, $f_\mu$, is modeled in terms of a turbulence Reynolds number, $Re_t=\rho k^2/\varepsilon\mu$. The turbulence transport equations for the *k*-ε model are defined as follows:
Turbulence energy transport equation:

$$\frac{\partial \rho k}{\partial t} + \frac{\partial}{\partial x_j}\left(\rho u_j \frac{\partial k}{\partial x_j} - \left(\mu + \frac{\mu_\tau}{\sigma_k}\right)\frac{\partial k}{\partial x_j}\right) = \tau_{tij}s_{ij} - \rho\varepsilon\,. \tag{8}$$

Energy dissipation transport equation:

$$\frac{\partial \rho \varepsilon}{\partial t} + \frac{\partial}{\partial x_j}\left(\rho u_j \varepsilon - \left(\mu + \frac{\mu_\tau}{\sigma_\varepsilon}\right)\frac{\partial \varepsilon}{\partial x_j}\right) = c_{\varepsilon 1}\frac{\varepsilon}{k}\tau_{tij}s_{ij} - c_{\varepsilon 2}\rho\frac{\varepsilon^2}{k}\,. \tag{9}$$

The model constants are defined as

$$c_\mu = 0.09\,,\ c_{\varepsilon 1} = 1.45\,,\ c_{\varepsilon 2} = 1.92\,,\ \sigma_k = 1.0\,,\ \sigma_\varepsilon = 1.3\,,\ Pr_t = 0.9\,. \tag{10}$$

#### 2.2.2.2 *k*-ω two-equation model (WILCOX, 1998)

The *k*-ω model is a well known and widely tested two-equation eddy viscosity model. Convective transport equations are solved for the turbulent kinetic energy and its specific dissipation rate, k and ω, respectively. The *k*-ω model has proven to be superior in numerical stability to the *k*-ε model primarily in the viscous sub-layer near the wall. In the logarithmic region, the model gives good agreement with experimental data for mild adverse pressure gradient flows. The Reynolds stresses are modeled in terms of the eddy viscosity as follows:

$$\tau_{tij} = 2\mu_t\left(s_{ij} - s_{nn}\delta_{ij}/3\right) - 2\rho k\delta_{ij}/3\,. \tag{11}$$

The eddy viscosity is defined as a function of the turbulent kinetic energy, *k*, and the specific rate of dissipation, *ω*, as follows:

$$\mu_t = \rho k/\omega\,. \tag{12}$$

The two transport model equations are defined as follows:
Turbulence energy transport equation:

$$\frac{\partial\rho k}{\partial t} + \frac{\partial}{\partial x_j}\left(\rho u_j k - \left(\mu + \sigma^*\mu_\tau\right)\frac{\partial k}{\partial x_j}\right) = \tau_{tij}s_{ij} - \beta^*\rho\omega k\,, \tag{13}$$

Specific dissipation rate equation:

$$\frac{\partial\rho\omega}{\partial t} + \frac{\partial}{\partial x_j}\left(\rho u_j\omega - \left(\mu + \sigma\mu_\tau\right)\frac{\partial\omega}{\partial x_j}\right) = \alpha\frac{\omega}{k}\tau_{tij}s_{ij} - \beta\rho\omega^2\,. \tag{14}$$

As described by Wilcox (1998), the model constants are defined as

$$\alpha = \frac{5}{9}\,,\ \beta = \frac{3}{40}\,,\ \beta^* = \frac{9}{100}\,,\ \sigma = 0.5\,,\ \sigma^* = 0.5\,,\ Pr_t = 0.9\,. \tag{15}$$

**2.2.2.3 *k*-ω SST two-equation model (Menter, 1994)**

The *k*-ω SST shear-stress-transport model combines several desirable elements of existing two-equation models. The two major features of this model are a zonal weighting of model coefficients and a limitation on the growth of the eddy viscosity in rapidly strained flows. The zonal modeling uses Wilcox's *k*-ω model near solid walls and the standard k-ε model near boundary layer edges and in free-shear layers. This switching is achieved with a blending function of the model coefficients. The eddy viscosity is defined as the following function of the turbulent kinetic energy, *k*, and the specific dissipation rate or turbulent frequency, ω:

$$\mu_t = \frac{\rho k/\omega}{\max\left[1, \Omega F_2/a_1\omega\right]}\,,\ a_1 = 0.31\,. \tag{16}$$

In turbulent boundary layers, the maximum value of the eddy viscosity is limited by forcing the turbulent shear stress to be bounded by the turbulent kinetic energy time $a_1$. This effect is achieved with an auxiliary function $F_2$ and the absolute value of the vorticity, Ω. The auxiliary function, $F_2$, is defined as a function of wall distance *y* as follows:

$$F_2 = \tanh\left\{\left(\max\left[2\frac{\sqrt{k}}{0.09\omega y}, \frac{500\mu}{\rho\omega y^2}\right]\right)^2\right\}. \tag{17}$$

The transport equation for the turbulent kinetic energy is

$$\frac{\partial\rho k}{\partial t} + \frac{\partial}{\partial x_j}\left(\rho u_j k - \left(\mu + \sigma_k\mu_\tau\right)\frac{\partial k}{\partial x_j}\right) = \tau_{tij}s_{ij} - \beta^*\rho\omega k \tag{18}$$

and the transport equation for the specific dissipation of turbulence is

$$\frac{\partial \rho\omega}{\partial t}+\frac{\partial}{\partial x_j}\left(\rho u_j\omega-\left(\mu+\sigma\mu_\tau\right)\frac{\partial \omega}{\partial x_j}\right)=p_\omega-\beta\rho\omega^2+2(1-F_1)\frac{\rho\sigma_{\omega 2}}{\omega}\frac{\partial k\partial\omega}{\partial x_j\partial x_j}, \tag{19}$$

where the last term of Eq. 19 represents the cross-diffusion term that appears in the transformed *k*-ω equation from the original *k*-ε equation. The production term of ω is sometimes approximated as proportional to the absolute value of vorticity, as follows:

$$p_\omega\equiv 2\gamma\rho\left(2s_{ij}-\omega s_{nn}\delta_{ij}/3\right)s_{ij}\approx\gamma\rho\Omega^2. \tag{20}$$

The function $F_1$ takes the value of one on no-slip surfaces and near one over a large portion of the boundary layer, and goes to zero at the boundary layer edge. This auxiliary blending function, $F_1$, is defined as

$$F_1=\tanh\left\{\left(\min\left[\max\left[\frac{\sqrt{k}}{0.09\omega y},\frac{500\mu}{\rho\omega y^2}\right],\frac{4\rho\sigma_{\omega 2}k}{CD_{k\omega}y^2}\right]\right)^4\right\}, \tag{21}$$

where

$$CD_{k\omega}=\max\left[2\rho\sigma_{\omega 2}\frac{1}{\omega}\frac{\partial k}{\partial x_j}\frac{\partial\omega}{\partial x_j},10^{-20}\right], \tag{22}$$

where $CD_{k\omega}$ stands for cross-diffusion in the *k*-ω model. The constants of the SST model are

$$a_1=0.31,\ \beta^*=0.09,\ \kappa=0.41. \tag{23}$$

The model coefficients β, γ, $\sigma_\kappa$ and $\sigma_\omega$ denoted with the symbol $\phi$ are defined by blending the coefficients of the original k-ω model, denoted as $\phi_1$, with those of the transformed k-ε model, denoted as $\phi_2$.

$$\phi=F_1\phi_1+(1-F_1)\phi_2,\ \text{where}\ \phi=\{\sigma_k,\sigma_\omega,\beta,\gamma\} \tag{24}$$

with the coefficients of the original models defined as
Inner model coefficients:

$$\sigma_{k1}=0.85,\ \sigma_{\omega 1}=0.5,\ \beta_1=0.075,\ \gamma_1=\beta_1/\beta^*-\sigma_{\omega 1}\kappa^2/\sqrt{\beta^*}=0.553. \tag{25}$$

Outer model coefficients:

$$\sigma_{k2}=1.0,\ \sigma_{\omega 2}=0.856,\ \beta_2=0.0828,\ \gamma_2=\beta_2/\beta^*-\sigma_{\omega 2}\kappa^2/\sqrt{\beta^*}=0.440. \tag{26}$$

### 2.2.3 Joule heating model

In general, Maxwell's equations should be solved in order to calculate Joule heating. However, if the current distribution of the arc heater is known, the Joule heating can be calculated using Ohm's law(the current distribution inside a constrictor is constant since the

constrictor wall is insulated electrically). With the assumption that the voltage gradient is independent of radius, Joule heating can be calculated as follows. Ohm's law for a cylindrical column is given by

$$j(x,y) = \sigma(x,y) \cdot E(x) \,, \tag{27}$$

where

$$E(x) = \frac{j(x,y)}{\sigma(x,y)} = \frac{\int_0^R 2\pi y j(x,y) dy}{\int_0^R 2\pi y \sigma(x,y) dy} = \frac{I}{\int_0^R 2\pi y \sigma(x,y) dy} \tag{28}$$

and

$$I = \int_0^R 2\pi y j(x,y) dy = const \tag{29}$$

from Kirchhoff's law of conservation of current. Finally, Joule heating can be calculated as

$$j(x,y) \cdot E(x) = \frac{I^2 \sigma(x,y)}{\left[\int_0^R 2\pi y \sigma(x,y) dy\right]^2} \,. \tag{30}$$

Figure 2 shows the typical current distribution in an arc heater along the axial direction.

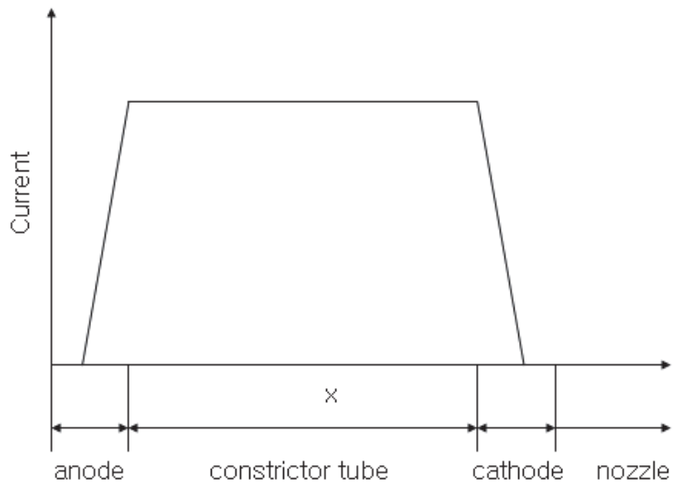


Fig. 2. Current Distribution in the Arc Heater

### 2.2.4 Radiation model

For high temperature flows, radiation becomes an important heat transfer mode in addition to thermal convection. The radiative transfer equation is as follows:

$$-\frac{1}{\rho \kappa_\nu} \frac{dI_\nu}{ds} = I_\nu - B_\nu \,, \tag{31}$$

where $I_\nu$ is the radiative intensity traveling along a ray denoted by, s. The absorption coefficient $\kappa_\nu$ is a function of frequency, temperature, and pressure; these are obtained from experiment. The Planck function $B_\nu$ is expressed as follows:

$$B_\nu = \frac{2h}{c^2}\frac{\nu^3}{e^{h\nu/kT}-1} \tag{32}$$

The radiant flux per unit frequency expressed in cylindrical coordinates can be calculated using Eq. 33, when the radiative intensity at a given point is calculated for all directions:

$$q_\nu(r) = \int_\Omega I_\nu(r)\cos\theta d\Omega \tag{33}$$

where θ is the angle between the ray and the outward normal to the cylindrical surface and Ω is the solid angle. The total radiative flux at any radius r can be expressed as,

$$q_R(r) = \int_0^\infty q_\nu(r)d\nu\ . \tag{34}$$

Under the band model assumption the total radiative flux can be written as,

$$q_R(r) = \sum_{l=1}^{m} q_l(r)\ , \tag{35}$$

where m is the total number of bands and $q_l(r)$ is the radiant flux contribution from the $l^{th}$ band to the total flux which is given by

$$q_l(r) = \int_{\Delta\nu_l} q_\nu(r)d\nu\ . \tag{36}$$

where $\Delta\nu_l$ is the band-width for the $l^{th}$ band. For accurate calculation of the radiant flux, a line-by-line calculation (Whiting et al., 1996) is the most desirable approach. However, such a line-by-line calculation requires a huge computational cost. Thus, Sakai and Olejniczak (2003) developed a new three band model that can compute radiative transport equations 400 times faster than the line-by-line calculation without losing accuracy. In this chapter, all calculations are performed by using this three-band radiation model. Details of the three band model are introduced in Sakai and Olejniczak (2003).

## 3. Validation of the CFD code

### 3.1 Validation

#### 3.1.1 NASA Interaction Heating Facility (IHF) arc heater

The IHF is operated with a 60 MW constricted arc heater that can operates at a pressure range of 1 to 9 atm and an enthalpy level of 7 to 47MJ/kg. In an experiment, Hightower et al. (2002) measured the performance of the IHF arc heater and Sakai and Olejniczak (2003) numerically calculated the flow inside the IHF arc heater. In this section, I compare the calculated results from ARCFLO4 with experimental data and from the data calculated by the ARCFLO3 code which is developed by Sakai and Olejniczak (2003). The calculated voltage, mass averaged enthalpy, chamber pressure, and efficiency are compared in terms of mass flow rate. Results are illustrated for the cases of I=3000A and 6000A. Figure 3 shows

calculated and experimental data for the case of I=3000A. The numerical results using three two-equation turbulence models are illustrated. As shown in the figure, the k-ε turbulence model predicted the operational data most accurately. It appears that k-ω turbulence model overestimated the mass-averaged enthalpy and efficiency. The k-ω SST turbulence model predicted mass-averaged enthalpy and chamber pressure fairly well, whereas the calculated voltage and efficiency deviated somewhat from the experimental data. That is, the combination of the k-ε turbulence model and the three-band radiation model seems to be appropriate for arc heater flow calculation.

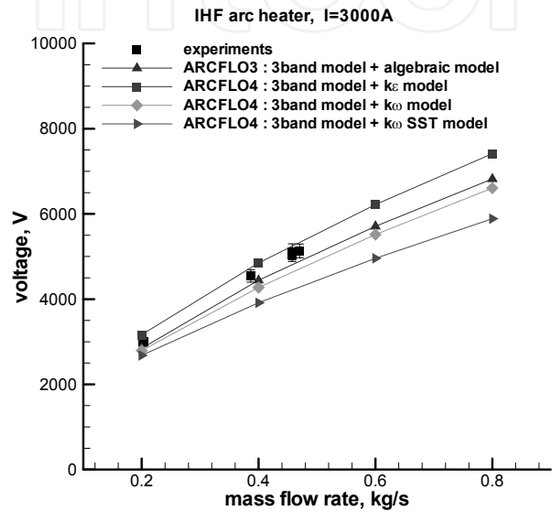


(a) Voltage

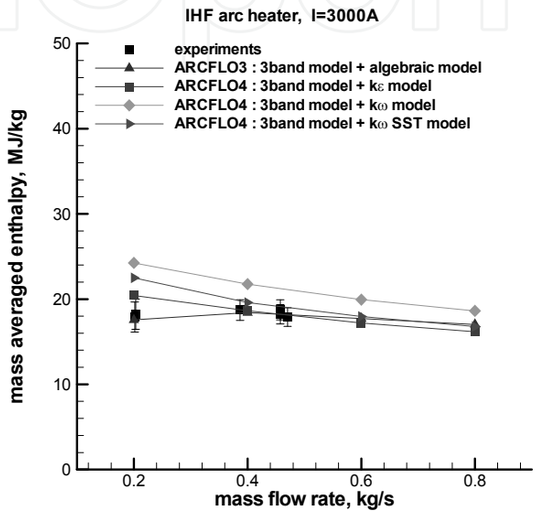


(b) Mass-Averaged Enthalpy

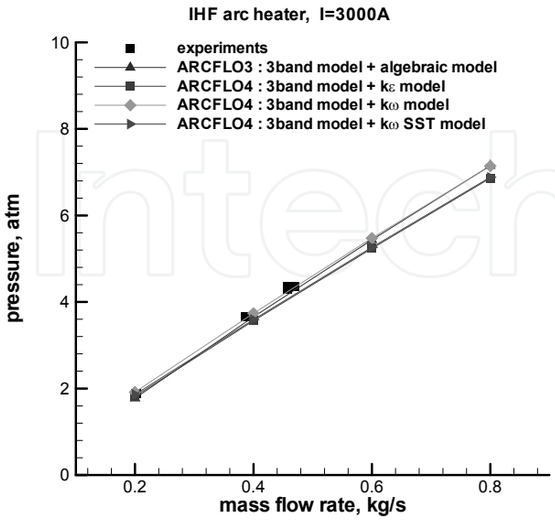


(c) Pressure

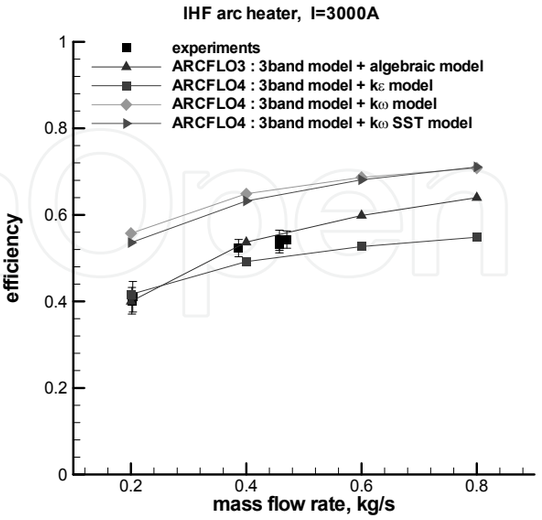


(d) Efficiency

Fig. 3. Comparison between Calculation and Experiment (Lee et al., 2007)

Figure 4 shows the results for I = 6000A. As shown in the figure, the overall results follow the same tendency as the case of I = 3000A. Again, the computational results of ARCFLO4 predicted the flow inside the arc heater accurately. The combination of the two-equation turbulence model and the three-band radiation model provide accurate performance parameters for the arc heater. Since the numerical solution using two-equation turbulence model does not require user experience for turbulent flows, it is expected that the numerical approach of ARCFLO4 can be applied to a wide range of arc heaters.

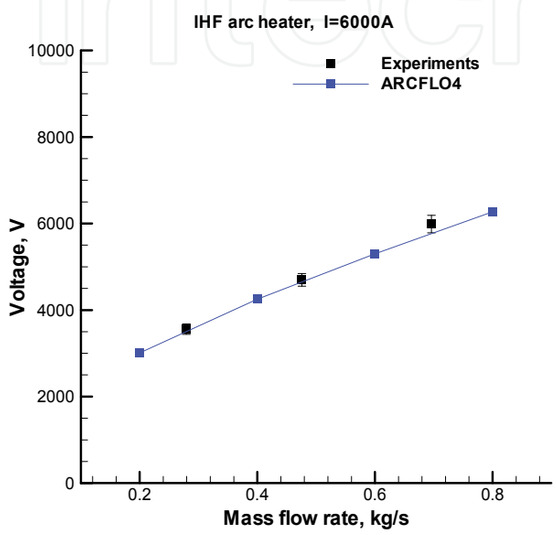


(a) Voltage

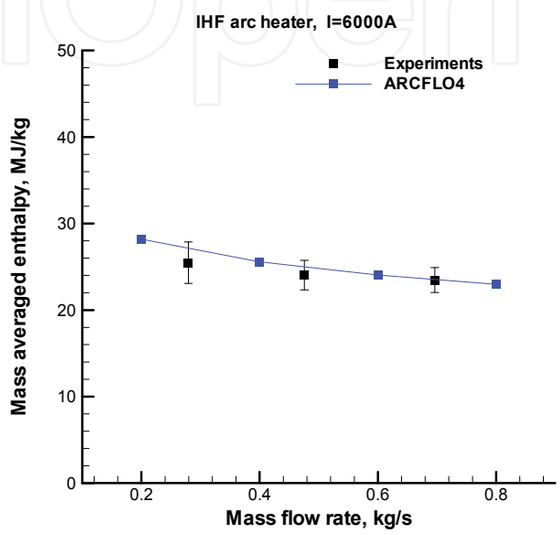


b) Mass-Averaged Enthalpy

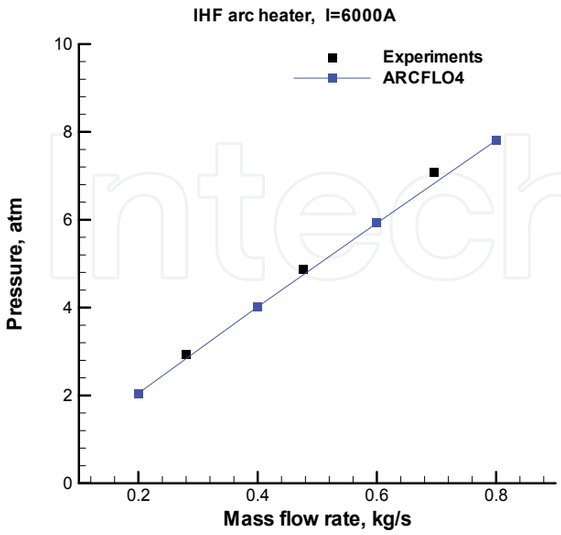


(c) Pressure

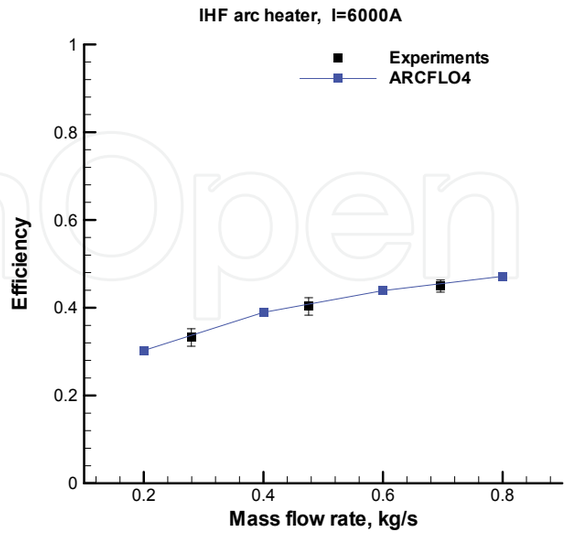


(d) Efficiency

Fig. 4. Comparison between Calculation and Experiment

### 3.1.2 NASA Aerodynamic Heating Facility (AHF) arc heater

The AHF is operated with a 20MW constricted arc heater that has a pressure range of 1 to 9atm and an enthalpy level of 1 to 33MJ/kg. Hightower et al. (2002) measured the performance of the AHF experimentally and Sakai and Olejniczak (2003) computed the corresponding flows using ARCFLO3. In this section, a comparison between computation and experiment is carried out in a manner similar way to previous IHF analyses. The calculated voltage, mass-averaged enthalpy, chamber pressure, and efficiency are compared using experimental data for the cases of I = 1600 and 2000 A. Figure 5 shows results for I = 1600 A. Similar to the IHF cases, the calculated results by ARCFLO4 are in good agreement with the experimental data.

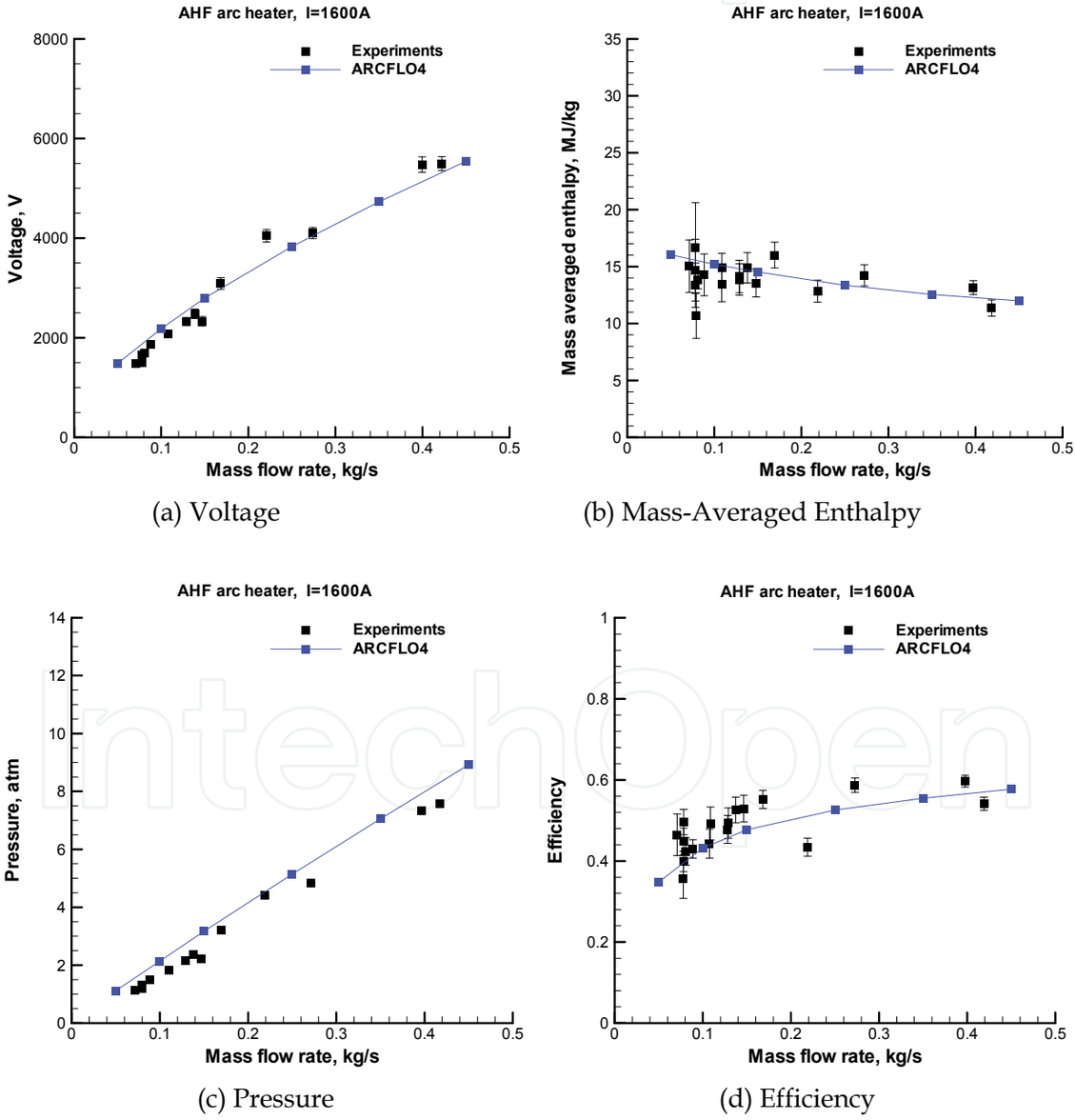


(a) Voltage (b) Mass-Averaged Enthalpy

(c) Pressure (d) Efficiency

Fig. 5. Comparison between Calculation and Experiment

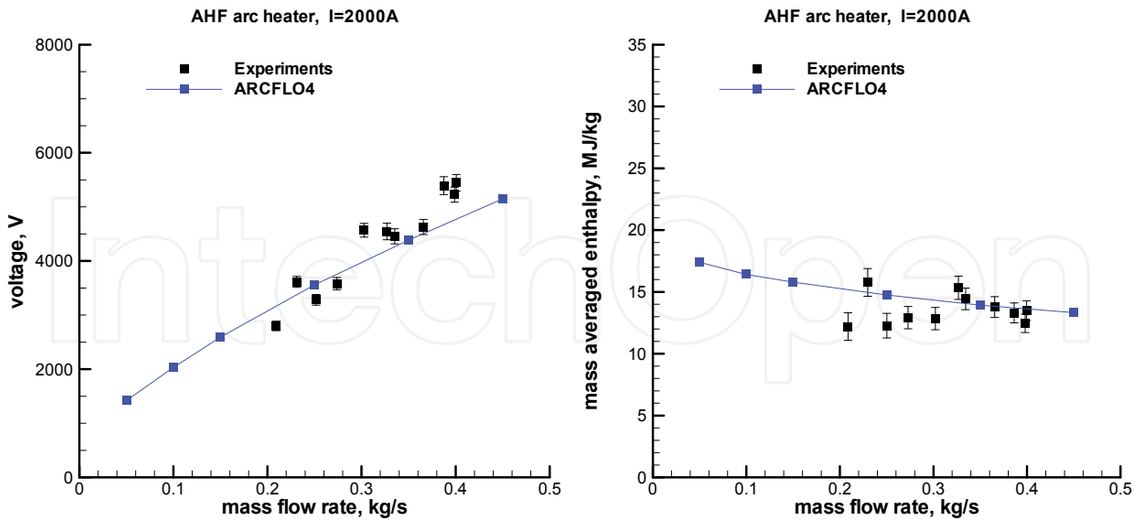


(a) Voltage (b) Mass-Averaged Enthalpy

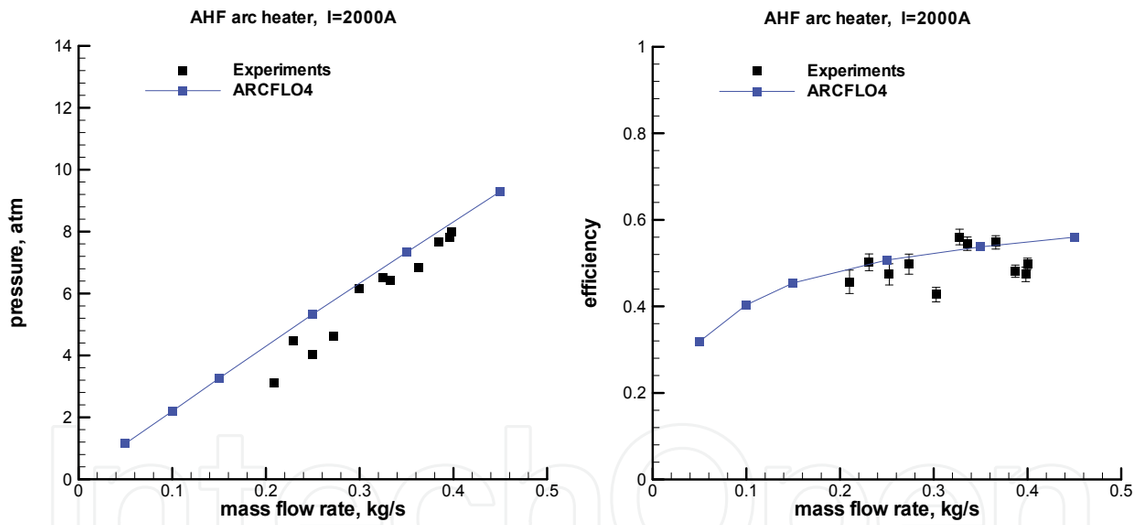


(c) Pressure (d) Efficiency

Fig. 6. Comparison between Calculation and Experiment

Figure 6 shows the results for I = 2000 A. As shown in the figure, the overall results show a tendency similar to the case of I = 1600 A and are in good agreement with the experimental results. Considering the results described in Sections 3.1.1 and 3.1.2, we can say that the ARCFLO4 code predicted the arc heater flow accurately for high electric power cases.

### 3.1.3 JAXA 750KW arc heater

The Japan Aerospace Exploration Agency (JAXA) has serviced a 750 kW segmented arc heater since the 1990s, and its operational data are available through the references of

Matsuzaki et al. (2002) and Sakai et al. (2007). The JAXA 750 kW segmented arc heater operates at a current between 300 and 700 A and a mass flow rate between 10 and 20 g/s. The constrictor length and diameter are 39 cm and 2.54 cm, respectively. The diameter of the nozzle throat is 2.5 cm. The diameter and the radius of the electrode is 7.6 cm and 1.9 cm, respectively. In this section, a numerical flow calculation of the JAXA 750 kW arc heater is introduced as a low electric power case. The voltage between electrodes, the mass-averaged enthalpy at the nozzle throat, the pressure in the cathode chamber, and the arc heater efficiency are calculated and compared to the experimental data.

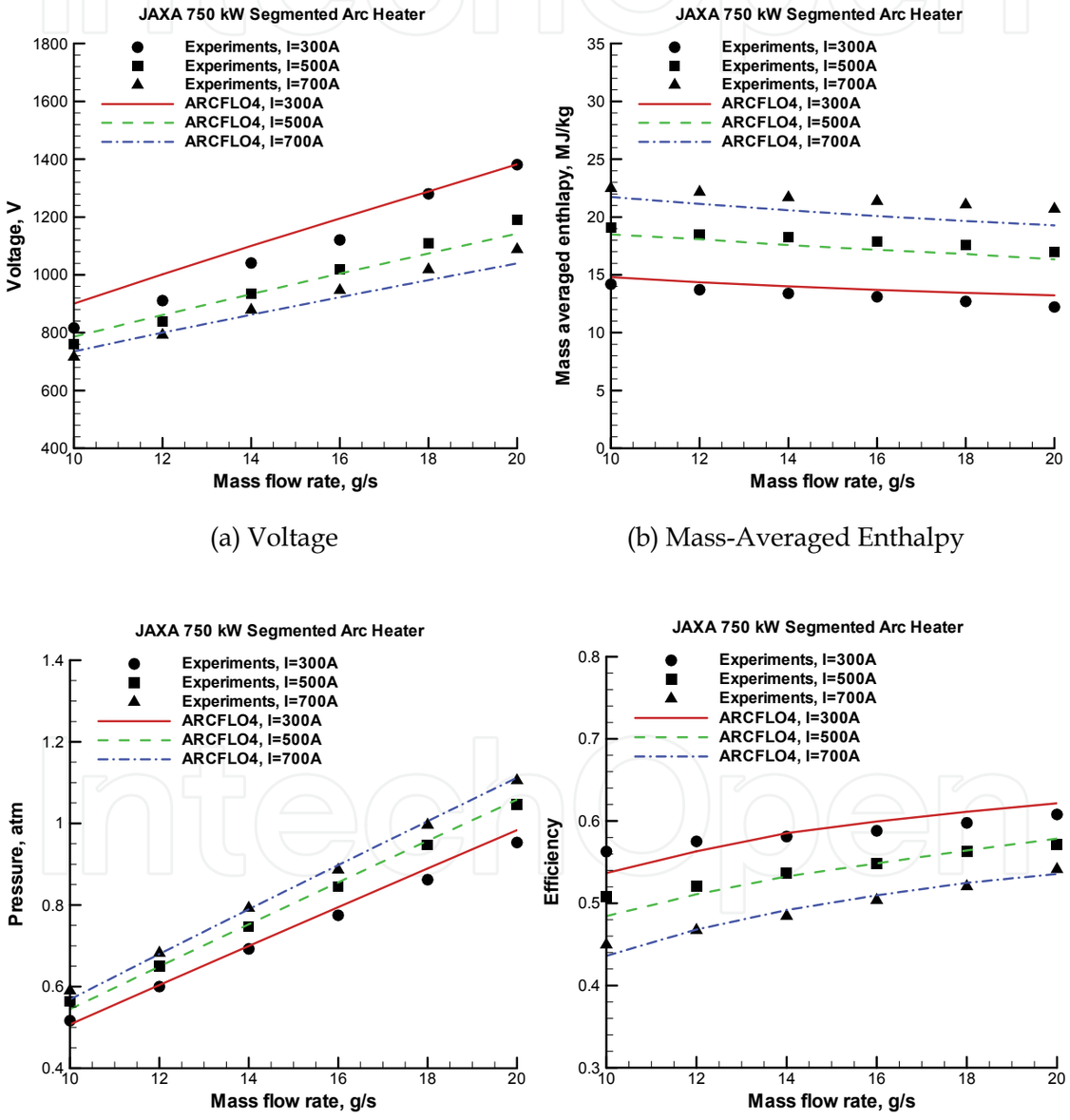


(a) Voltage

(b) Mass-Averaged Enthalpy

(c) Pressure

(d) Efficiency

Fig. 7. Comparison between Calculation and Experiment (Lee & Kim, 2010)

Figure 7 shows a comparison of the operational data plotted in terms of mass flow rates. As shown in the figure, the computed operational data are in good agreement with the experimental data. Thus, it is confirmed that the ARCFLO4 simulation of low electric power segmented arc heater flows is valid.

### 3.1.4 150KW arc heater

A 150 kW arc heater in Korea was analyzed in order to validate ARCFLO4 for a lower electric power regime. This arc heater is basically a Hules-type heater. However, to stabilize the arc, the constrictor is located at the center of the heater. The details of the configurations are shown in Fig. 8, and the test cases for present analysis are given in Table 1.

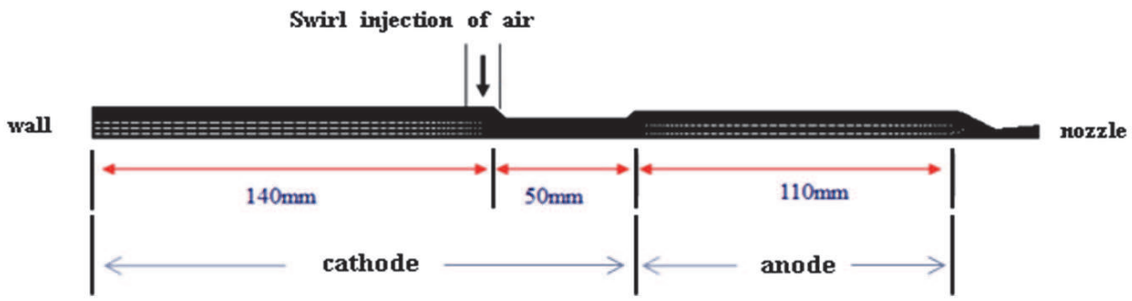


Fig. 8. Computational Grid

| | Current(Amphere) | Mass flow rate(g/s) |
|---|---|---|
| CASE1 | 363 | 11.78 |
| CASE2 | 393.3 | 10.11 |
| CASE3 | 383 | 9.08 |
| CASE4 | 374.4 | 7.53 |

Table 1. Test Cases

Generally, radiant heat flux is mainly generated at the constrictor and has almost zero value at the cathode and anode for the case of a long constrictor. Therefore, the ARCFLO4 code calculates the radiant flux using the assumption of long cylindrical coordinates. However, this 150 kW arc heater has a relatively short constrictor length, so the assumption is not valid. Considering the short length of the constrictor, the calculation of radiant flux was slightly corrected using a configuration factor, as shown in Fig. 10. The details of the correction are available in Han et al., 2011.

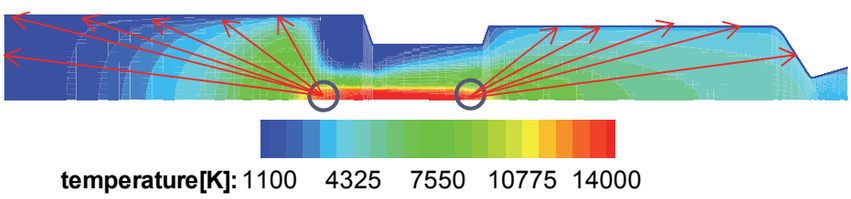


Fig. 9. Correction of Radianit Heat Flux Using Configuration Factor (Han et al., 2011)

Table 2 shows a comparison of the ARCFLO4 numerical results and the experimental results. The table shows that the calculated voltage and pressure are in very good agreement with the experimental data. That is, ARCFLO4 showed good accuracy again for the flow inside the low electric power arc heater.

| | Pressure(atm) | | | Voltage(volt) | | |
|---|---|---|---|---|---|---|
| | Cal. | Exp. | Error | Cal. | Exp. | Error |
| Case1 | 6.25 | 6.33 | 1.3% | 385 | 392 | 2.8% |
| Case2 | 5.62 | 5.60 | 0.35% | 345 | 344 | 0.3% |
| Case3 | 5.05 | 4.93 | 2.4% | 328 | 320 | 2.5% |
| Case4 | 4.41 | 4.56 | 3.1% | 325 | 335 | 2.8% |

Table 2. Comparisons between Calculations and Experiments (Han et al., 2011)

Considering the results described in Sections 3.1.1 to Sec. 3.1.4, the ARCFLO4 code predicted the flow inside the arc heater accurately for a wide range of electric power (150 kW to 60 MW). It is also confirmed that the turbulence model used in ARCFLO4 reflected the convection physics of turbulence properly near the wall region.

## 4. CFD code as a design tool of the arc heater

The NASA Ames Research Center developed a segmented arc heater in the 1960s. Currently, NASA Ames has three segmented arc heater facilities: the 20 MW Aerodynamic Heating Facility, the 20 MW Panel Test Facility, and the 60 MW Interactive Heating Facility (Terrazas-Salinas and Cornelison, 1999). In the 1990s, Europe and Japan began to develop segmented arc heaters. In Europe, a 6 MW segmented arc heater was developed and operated with an L3K arc heated facility of the German Aerospace Center (Smith et al., 1996). Recently, 70 MW segmented arc heater was added to the SCIROCCO arc heated facility of the Italian Aerospace Research Center (Russo, 1993). Japan has serviced the 750 kW segmented arc heater since the 1990s. Despite these arc heater development experiences, a design process has been accomplished by only a few research centers and companies. In the development stage, there was probably considerable trial and error since the flow phenomena inside segmented arc heaters had not been characterized. Also, the higher cost would have been spent during the development of the segmented arc heater. In an effort to reduce the difficulties and cost during arc heater development, Lee et al. (2007, 2008) recently developed the ARCFLO4 computational code to study the flow physics in segmented arc heaters. As described in Section.3, the code accurately simulated existing arc heaters under various operating conditions. It predicted well the operational data of the AHF, IHF (Lee et al., 2007, 2008) and JAXA 750 kW arc heater (Lee & Kim, 2010). Since ARCFLO4 can accurately predict operational data and the wall heat energy loss, development costs can be reduced without previous design experience.

In this section, the effects of configuration and input operational conditions on the performance of an arc heater are investigated in order to provide fundamental data for the design of segmented arc heaters. A parametric study is performed to determine the main design variables that strongly affect arc heater performance. First, performance changes in terms of constrictor length, constrictor diameter, and nozzle throat diameter are investigated. Then, performance changes due different input currents and mass flow rates are examined.

### 4.1 Parametric study

The relationship between performance and main design parameters, such as configuration and input operational conditions is investigated. The 750 kW JAXA segmented arc heater is chosen as a baseline model. To study the effect of configuration on arc heater flows, a constrictor length, a constrictor diameter, and a nozzle throat diameter are changed. Then, the input current and mass flow rate are changed to determine the effect of input operational conditions on arc heater flows.

#### 4.1.1 Length of the constrictor

Generally, the arc length inside a segmented arc heater is similar to the constrictor length. Thus, the constrictor length is one of the key factors that affects arc heater flows. In this section, a parametric study according to the various constrictor lengths is described. The constrictor length varies from 10 to 100 cm with other parameters are fixed for comparison. In order to maintain an input electric power lower than 1 MW, a current of 300 A and a mass flow rate of 10 g/s were selected. The nozzle throat diameter is 1.5 cm. Figure 10 shows

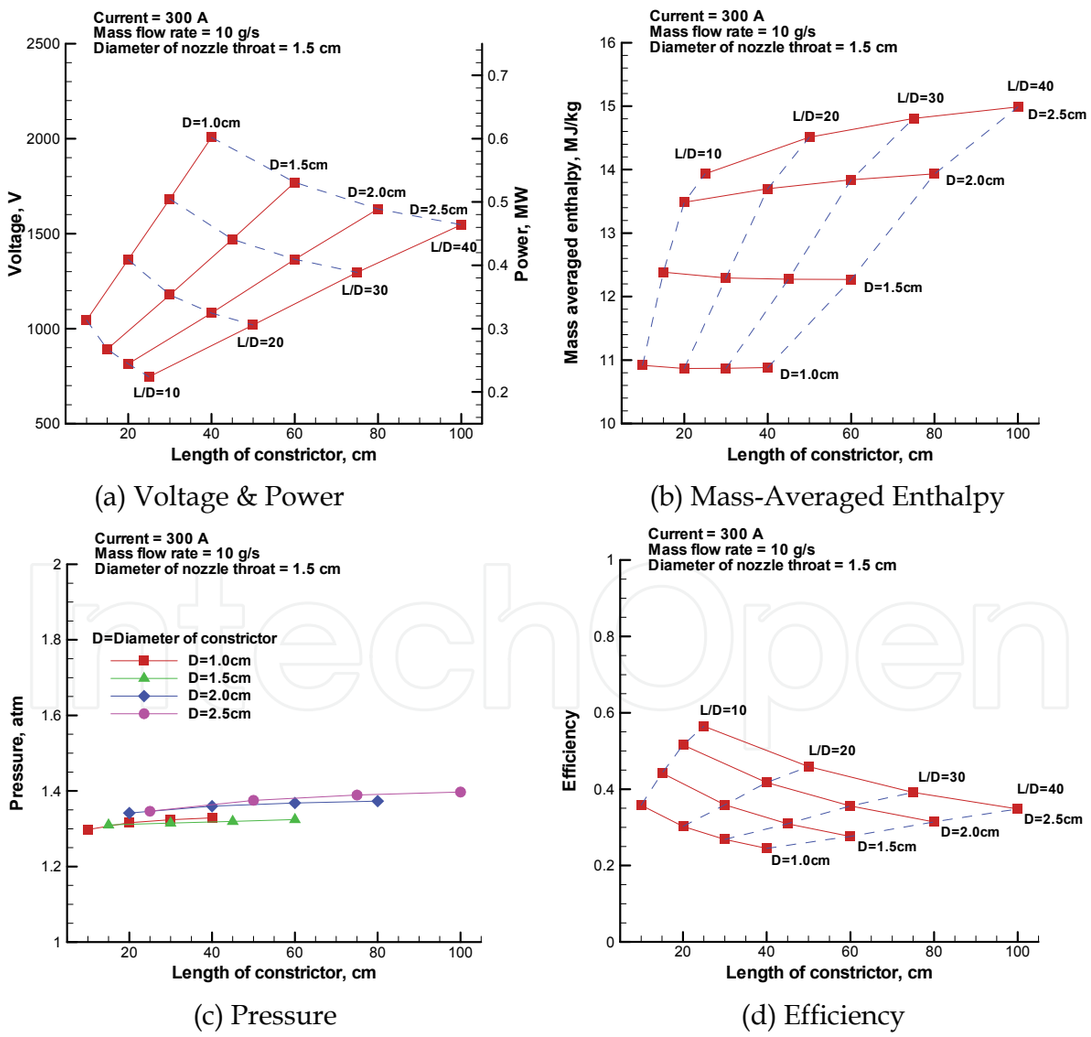


(a) Voltage & Power

(b) Mass-Averaged Enthalpy

(c) Pressure

(d) Efficiency

Fig. 10. Operational Data (Lee & Kim, 2010)

operational data in terms of a constrictor length at specific constrictor diameters. As shown in Fig. 10a, the voltage and the electric power are increased proportionally to the constrictor length. On the other hand, as shown in Figs. 10b and 10c, the effects of constrictor length on the mass-averaged enthalpy and the cathode chamber pressure are relatively small. It is shown that the efficiency decreases as the constrictor length increases. In general, the efficiency is strongly related to the amount of heat energy loss at the arc heater wall. The heat energy loss per unit length increases and the electric power input per unit length decreases, by increasing the constrictor length. Therefore, the longer the constrictor length, the lower the total efficiency becomes.

### 4.1.2 Diameter of the constrictor

The effects of the constrictor diameters are also investigated. The constrictor diameters vary from 1.0 to 6.0 cm, while other configurations are fixed. The nozzle throat diameter is 1.5 cm. The current and mass flow rate are also fixed at 300 A and 10 g/s, respectively. Figure 11

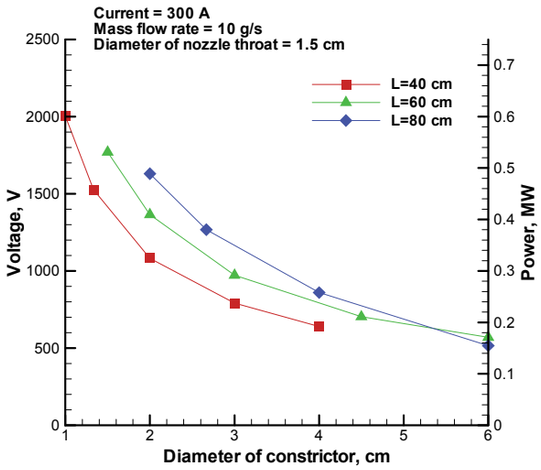


(a) Voltage & Power

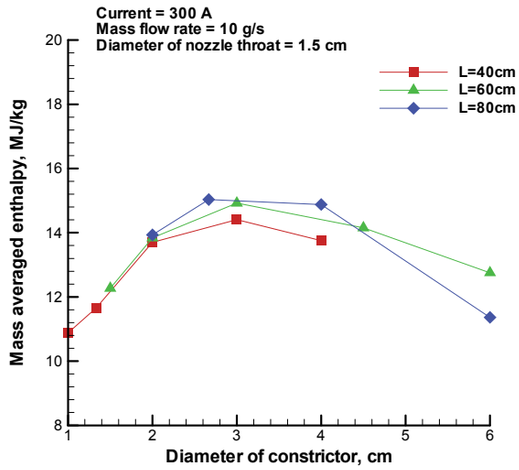


(b) Mass-Averaged Enthalpy

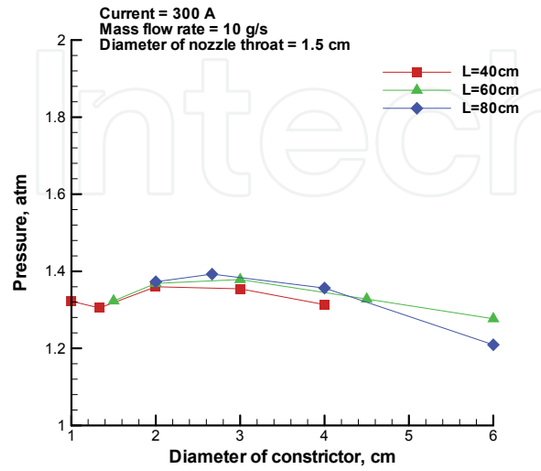


(c) Pressure

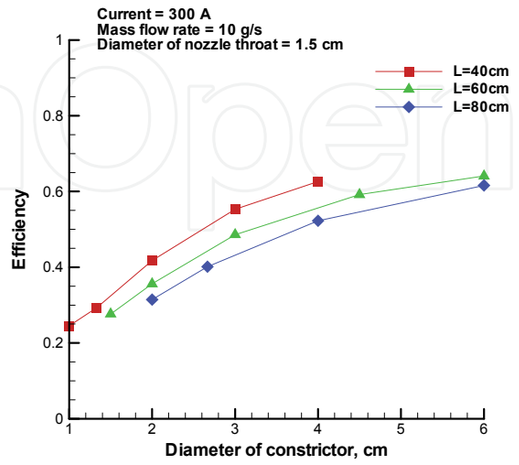


(d) Efficiency

Fig. 11. Operational Data (Lee & Kim, 2010)

shows operational data in terms of constrictor diameter. As shown in the figure, the voltage, mass-averaged enthalpy, and efficiency are strongly affected by the constrictor diameter. As shown in Fig. 11a, the voltage and the electric power increase as the constrictor diameter decreases. For the mass-averaged enthalpy, the effect of the constrictor diameter is greater than that of the constrictor length, as shown in Figs. 10b and 11b. In Fig. 11c, we note that the cathode chamber pressure is weakly affected by the constrictor diameter. Finally, Fig. 11d shows that the efficiency decreases as the constrictor diameter decreases.

To understand the change in efficiency, we consider the heat energy loss on the arc heater wall as illustrated in Fig. 12. In the figure, as the constrictor diameter decreases, both the conductive and radiant energy losses increase, and thus the efficiency decreases. Generally, if a constrictor diameter decreases, the quantity of injecting working gas per unit area increases. Thus, the axial speed of the working gas increases, and thus a viscous dissipation phenomenon due to turbulence is strongly generated near the wall. Therefore, the heat energy loss by thermal conduction increases as the constrictor diameter decreases. Moreover, the distance from the core to the wall is small; thus, only a small amount of radiation is absorbed by the surrounding gas on its way to the wall.

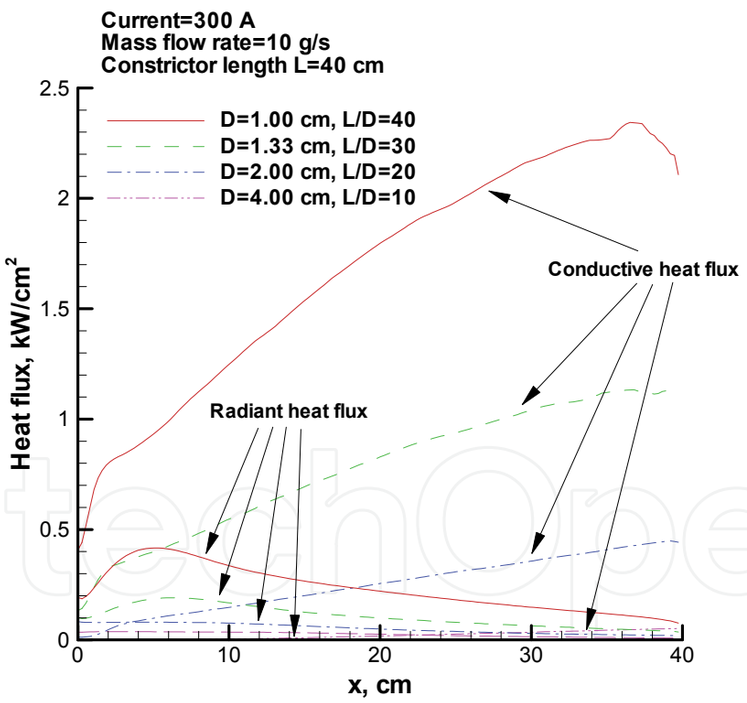


Fig. 12. Heat Flux (Lee & Kim, 2010)

The effect of the ratio of constrictor length to constrictor diameter, L/D, on the stability of an arc discharge is investigated. Figure 13 shows the temperature distribution in the radial direction. In the figure, we can define a region where the temperature is greater than 9,000 K and the current density is high, as an arc column. It is shown that the thickness of the arc column is large at the upstream region of the constrictor where L/D is greater than 30. Also,

the arc column broadens as L/D increases. If an arc column broadens, there is not enough room for the arc column to fluctuate and the stability of an arc discharge improves. Generally, it is known that L/D should be greater than 30 to stabilize an arc discharge (Sakai et al., 2007).

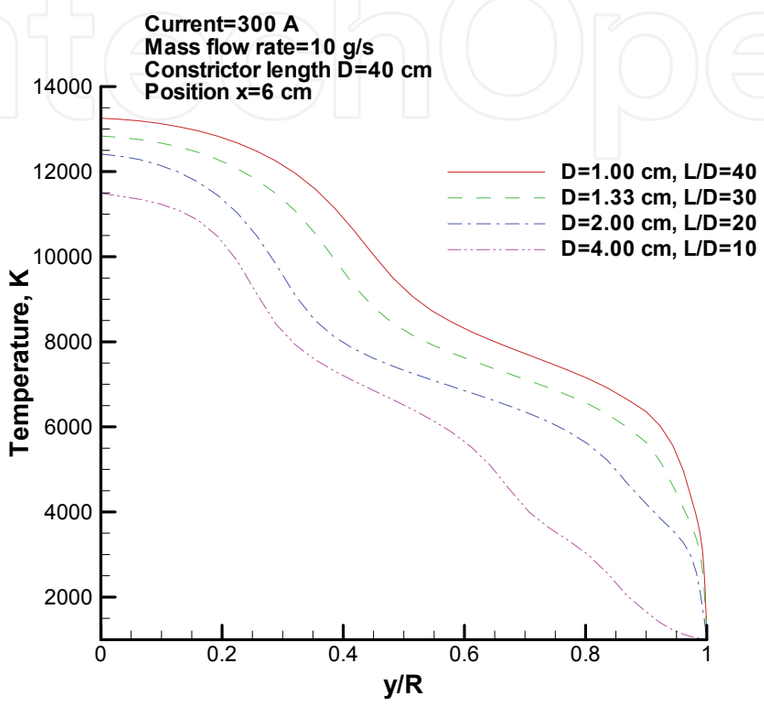


Fig. 13. Temperature (Lee & Kim, 2010)

### 4.1.3 Diameter of nozzle throat

To investigate the effect of nozzle throat diameter on the arc heater flow, the nozzle throat diameter is chosen to vary from 1.0 to 2.0cm, while other parameters are fixed. The length and the diameter of the constrictor are 60.0 cm and 2.0 cm, respectively. Figure 14 shows operational data in terms of the nozzle throat diameter. As shown in the figure, the nozzle throat diameter does not affect operational data, such as electric voltage, mass averaged enthalpy, and efficiency. However, the chamber pressure is strongly affected by the nozzle throat diameter since the pressure is inversely proportional to nozzle area for a fixed mass flow rate. The pressure decreases as the nozzle throat diameter increase.

### 4.1.4 Input current

When designing a segmented arc heater, a range of input currents must be determined as well as arc heater configurations. In this section, the effects of the input current on arc heater flow are investigated. The input current is defined to vary from 100 to 900 A. The length and the diameter of the constrictor are 60.0 cm and 2.0 cm, respectively. The diameter of the nozzle throat is 1.5 cm.

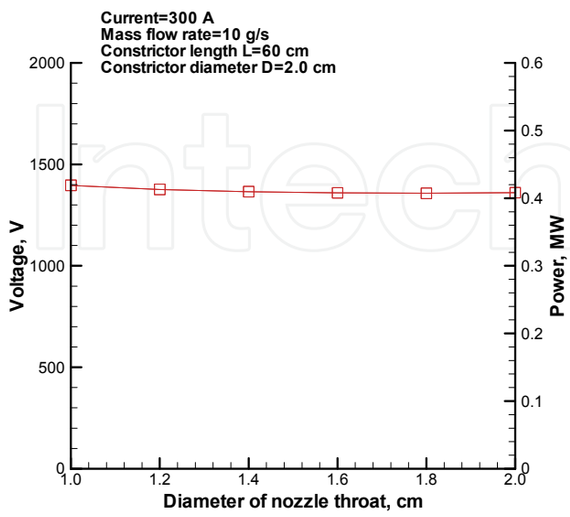


(a) Voltage & Power

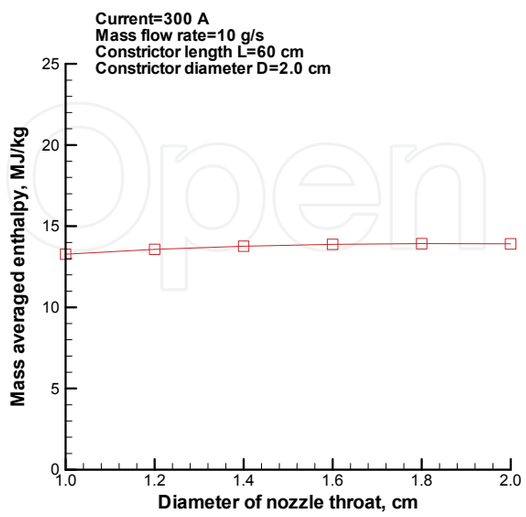


(b) Mass-Averaged Enthalpy

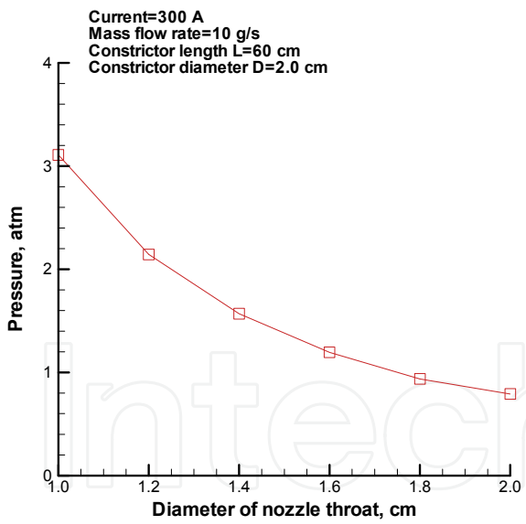


(c) Pressure

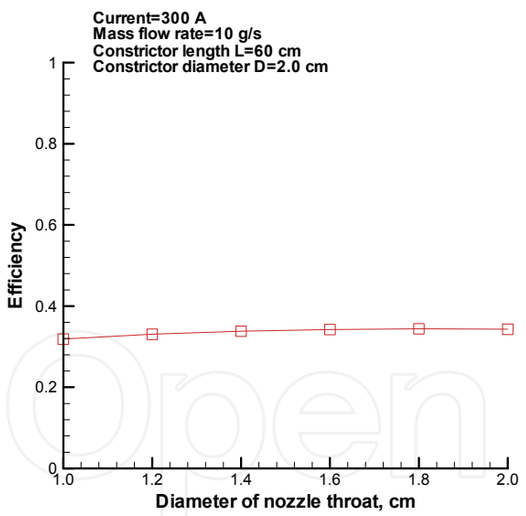


(d) Efficiency

Fig. 14. Operational Data (Lee & Kim, 2010)

Figure 15 shows operational data in terms of input current at the following mass flow rates: 10, 15, and 20 g/s. Figure 15a shows that the electric power is almost proportional to the input current, while the voltage decreases as the input current increases. The reason is that constrictor length dominantly determines the voltage value. Accordingly, the mass-averaged enthalpy and pressure increase under the condition of constant mass flow rate, as shown in Figs. 15b and c. Efficiency decreases as the input current increases.

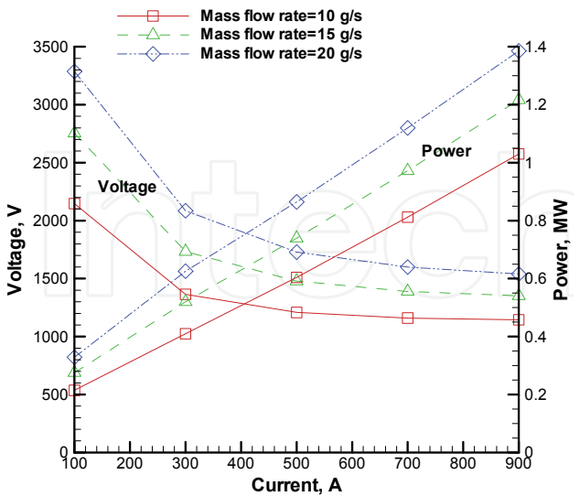


(a) Voltage & Power

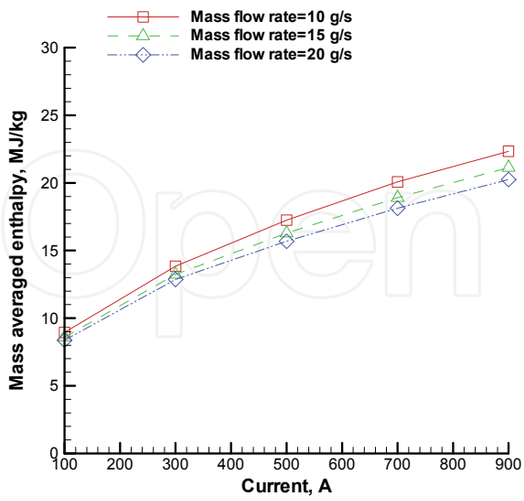


(b) Mass-Averaged Enthalpy

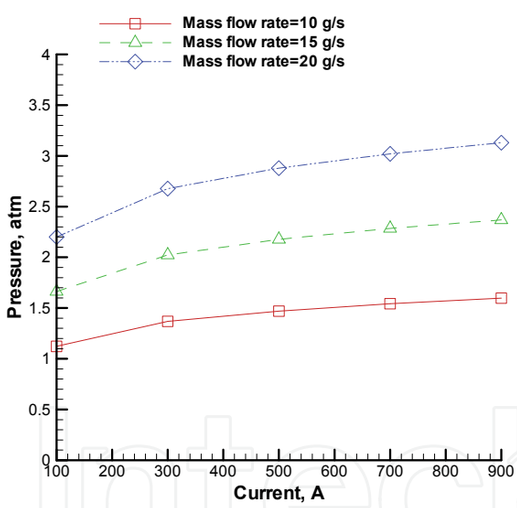


(c) Pressure

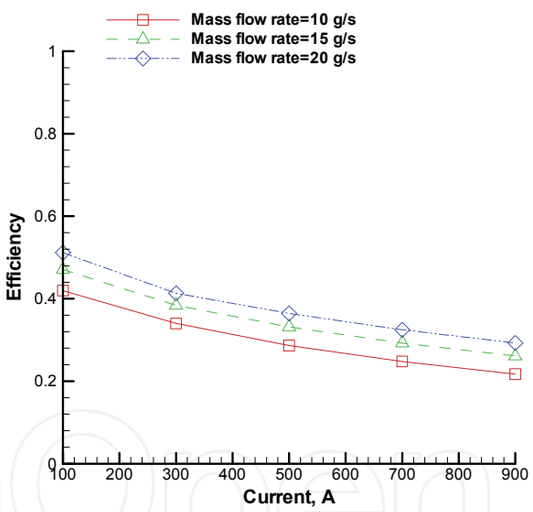


(d) Efficiency

Fig. 15. Operational Data (Lee & Kim, 2010)

Efficiency is strongly related to temperature distribution. As the input current increases, the core temperature increases and the arc column broadens. Generally, if the current increases, the temperature increases due to high Joule heating. On the other hand, strong radiation prohibits the core temperature from increasing. Instead, it makes the temperature distribution to be flat at the core region and arc column broader, which leads to enhanced radiation throughout the wall. Also, the temperature gradient near the wall increases, which increases the heat energy loss by thermal conduction. As a consequence, efficiency decreases due to high heat energy loss caused by radiation and thermal conduction.

### 4.1.5 Mass flow rate

A parametric study according to a mass flow rate is performed. The mass flow rate changes from 5 to 30 g/s. The length and diameter of the constrictor are 60.0 cm and 2.0 cm, respectively. The diameter of the nozzle throat is 1.5 cm. Figure 16 shows operational data in terms of the mass flow rate for three input currents: 300, 500, and 700 A. Figure 16a shows that the voltage and the electric power increase as the mass flow rate increases. This is

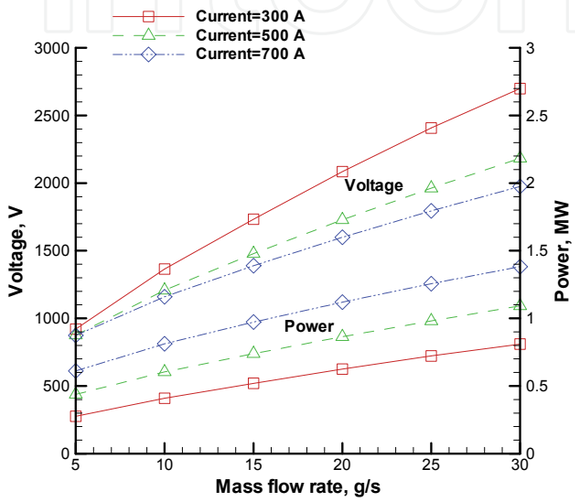


(a) Voltage & Power

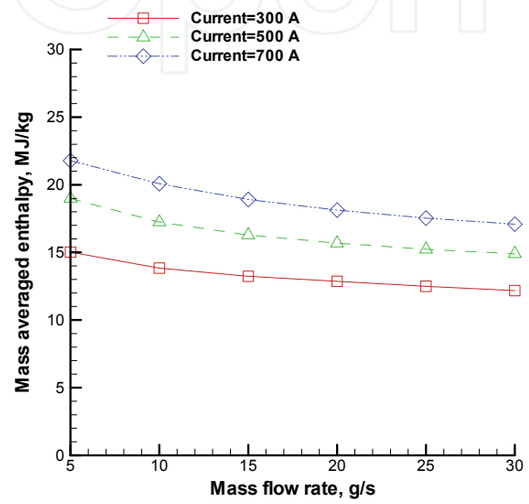


(b) Mass-Averaged Enthalpy

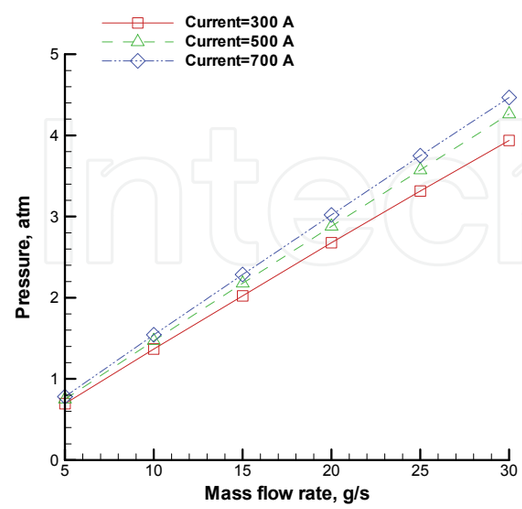


(c) Pressure

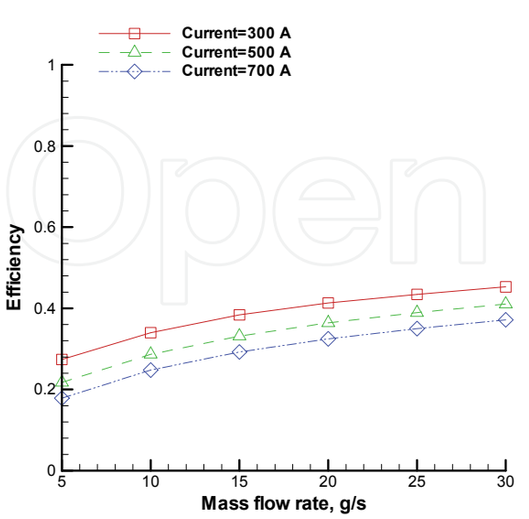


(d) Efficiency

Fig. 16. Operational Data (Lee & Kim, 2010)

because that the ionization rate decreases due to the high mass flow rate inside the arc column. As shown in Fig. 16b, the mass-averaged enthalpy decreases as the mass flow rate increases. On the other hand, in Fig. 16c, the cathode chamber pressure increases as the mass flow rate increases. In addition, efficiency increases as the mass flow rate increases. Figure 17 shows the temperature distribution along the radial direction at the middle cross section, which is 30 cm from the constrictor starting point. As shown in the figure, the core temperature decreases and the arc column becomes narrower as the mass flow rate increases. This temperature distribution makes the voltage higher and reduces the energy loss due to radiation, as shown in Fig. 18. On the other hand, viscous dissipation by turbulence occurs noticeably near the wall due to the high mass flow rate and high axial speed of the working gas. Hence, both the temperature gradient near the wall and the heat energy loss due to thermal conduction increase, as shown in the Fig. 18. Consequently, the more the mass flow rate increases, the higher the total energy loss becomes. However, as a result, the efficiency increases slowly along with the increase in mass flow rate because the total heat energy loss increases more slowly than the total electric power input.The mass flow rate also has an influence on the stability of arc discharge. Figure 17 shows that the arc column becomes narrower with increased mass flow rate. That is, the stability of the arc discharge becomes worse as the mass flow rate increases. In a real design process, the maximum value of the mass flow rate should be determined considering the stability of the arc discharge for a given arc heater configuration.

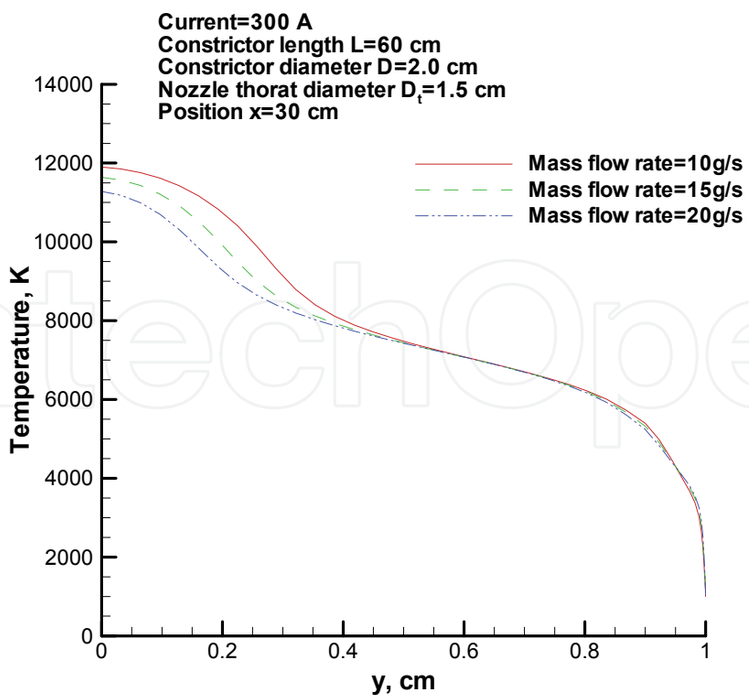


Fig. 17. Temperature (Lee & Kim, 2010)

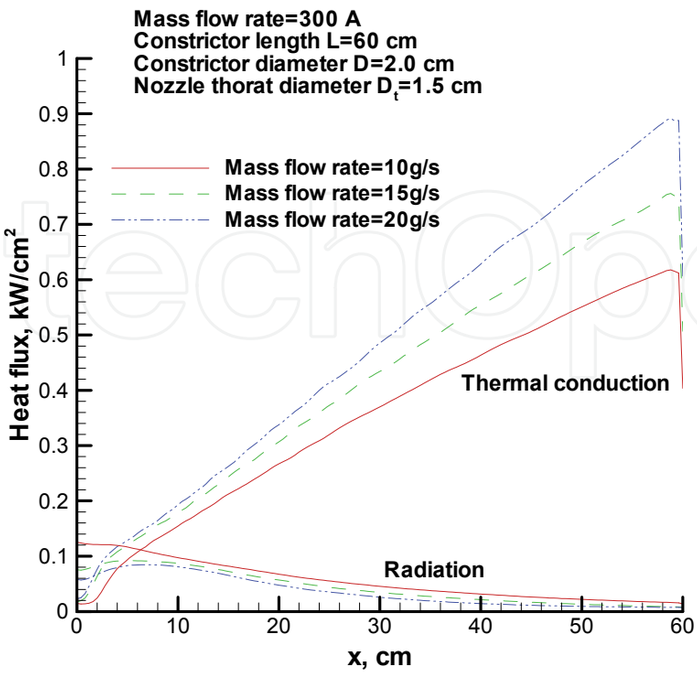


Fig. 18. Heat Flux (Lee & Kim, 2010)

### 4.2 Design of a segmented arc heater

In Section 3, the numerical code, ARCFLO4, is validated using the real operating data of the arc heater. In Section 4.1, a parametric study is performed for the various design parameters of the arc heater. Since the accuracy of the numerical results is rigorously proven, the database obtained by the parametric study is quite reliable. Therefore, it is expected that the database can be used in arc heater design processes. If target parameters such as total pressure and total enthalpy are given, the configuration and operational conditions such as the size of the constrictor and the nozzle throat, and the range of the input current and the mass flow rate, can be directly determined through the database based on the parametric study. Moreover, in the design of a cooling system, the database can be effectively used since the CFD code predicts the wall heat flux value quite well, i.e., if the heat flux value on the arc heater is known, the size of the cooling system and pipe configuration can be determined directly.

## 5. Conclusion

The accuracy level of current CFD analysis on arc heater flows is introduced. It is shown that current state-of-the art CFD technologies can predict the plasma flow inside the arc heater well. Both the high input power cases (60MW, 20MW) and the low input power cases (750kW, 150kW) are validated successfully using the ARCFLO4 computational code. The k-ε turbulence model combined with the 3-band radiation model provides good solutions for arc heater flows. Moreover, the possibility of the present computational code as a design tool for arc heater is introduced. A parametric study is performed to investigate the relation between arc heater performance and the design parameters. In the case of constrictor length,

as the constrictor length increases, the voltage and electrical power increase while the efficiency decreases. It is also shown that the voltage, the mass-averaged enthalpy, and the efficiency are strongly affected by the constrictor diameter. The mass-averaged enthalpy seems to be affected more by the constrictor diameter than by the constrictor length. From the view point of arc stability, as the L/D ratio increases, the arc column broadens, which means that the stability of the arc improves. Based on a parametric study of the nozzle throat diameter, it is determined that the nozzle throat diameter strongly affects the pressure. The effects of input operational conditions such as input current and mass flow rate are also discussed. It appears that the electric power increases as the input current and the mass flow rate increase. Moreover, arc stability becomes worse as the mass flow rate increases or the input current decreases. It appears that if the configuration of the arc heater is known, the minimum value of input current and maximum value of the mass flow rate can be determined using the numerical parametric study results. Therefore, it is expected that the ARCFLO4 code could play an important role in the design process of arc heater.

## 6. Acknowledgement

The authors would like to specially thank Chul Park for a technical guidance at the Korea Advanced Institute of Science and Technology. The authors would like to also thank Takehara Sakai for an offer of his three-band radiation code at the Nagoya University.

## 7. References

Gupta, R. N., Yos, J. M., Thompson, R. A., & Lee, K. P. (1990). A Review of Reaction Rates and Thermodynamic and Transport Properties for an 11-Species Air Model for Chemical and Thermal Nonequilibrium Calculations to 30000 K, NASA RP-1232, August 1990.

Han, S. H., Byeon, J. Y., Lee, J. I, & Kim, K. H. (2011). Numerical analysis of a 150kW enhanced Huels type arc heater, 49th AIAA aerospace science meeting, Orlando, January 2011.

Hightower, T. M., Balboni, J. A., MacDonald, C. L., Anderson, K. F., & Martinez, E. R. (2002). Enthalpy by Energy Balance for Aerodynamic Heating Facility at NASA Ames Research Center Arc Jet Complex, 48th International Instrumentation Symposium, the Instrumentation, Systems, and Automation Society, Research Triangle Park, NC, May 2002.

Jameson, A. & Yoon, S. (1987). Lower-Upper Implicit Schemes with Multiple Grids for the Euler Equations, AIAA Journal, Vol. 25, No. 7, 1987, 929-935.

Jones, W. P., & Launder, B. E. (1972). The Prediction of Laminarization with a Two-Equation Model of Turbulence, International Journal of Heat and Mass Transfer, vol. 15, No. 2, 1972, 301–314.

Kim, K. H. & Kim, C. (2005). Accurate, efficient and monotonic numerical methods for multi-dimensional compressible flows Part II: Multi-dimensional limiting process, Journal of Computational Physics, Vol. 208, No. 2, September 2005.

Kim, J. G., Oh, J. K., & Park, C. (2006). A High Temperature Elastic Collision Model for DSMC Based on Collision Integrals, AIAA paper 2006-3803, June 2006.

Kim, K. H., Rho, O. H., & Park, C. (2000). Navier-Stokes Computation of Flows in Arc Heaters, Journal of Thermophysics and Heat Transfer, Vol. 14, No. 2, 2000, 250-258.

Kim, K. H., Kim, C., & Rho, O. H. (2001). Methods for the Accurate Computations of Hypersonic Flows: I. AUSMPW+ Scheme, Journal of Computational Physics, Vol. 174, No.1, November 2001, 38-80.

Lee, J. I., Kim, C., & Kim, K. H. (2007). Accurate Computations of Arc-heater Flows Using Two-equation Turbulence Models, Journal of Thermophysics and Heat Transfer, Vol. 21. No. 1, 2007, 67-76.

Lee, J. I., Han, S. H., Kim, C., & Kim, K. H. (2008). Analysis of Segmented Arc-heater Flows with High Argon Concentration, Journal of Thermophysics and Heat Transfer, Vol. 22, No. 2, 2008, 187-200.

Lee, J. I. & Kim, K. H. (2010). Numerical Parameter Study of Low Electric Power Segmented Arc Heaters, AIAA 2010-230, January 2010.

Matsuzaki, T., Ishida, K., Watanabe, Y., Miho, K., Itagaki, H., & Yoshinaka, T. (2002). Construction and Characteristics of the 750 kW Arc Heated Wind Tunnel, Rept. TM-760, October 2002.

McBride, B. J., Zehe, M. J., & Gordon, S. (2002). NASA Glenn Coefficients for Calculating Thermodynamic Properties of Individual Species, NASA TP 2002-211556, September 2002.

Menter, F. R. (1994). Two-Equation Eddy Viscosity Turbulence Models for Engineering Applications, AIAA Journal, Vol. 32 No. 8, Nov. 1994, 1598-1605.

Nicolet, W. E., Shepard, C. E., C. E., Clark, K. J. Balakrishnan, A., Kesselring, J. P., Suchsland, K. E., & Reese, J. J. (1975). Analytical and Design Study for a High-Pressure, High-Enthalpy Constricted Arc Heater, AEDC-TR-75-47, July 1975.

Park, C. (2001). Chemical-Kinetic Parameters of Hyperbolic Earth Entry, Journal of Thermophysics and Heat Transfer, Vol. 15, No. 1, 2001, 76-90.

Russo, G. (1993). The Scirocco Wind Tunnel Project - Progress report 1993, AIAA Paper 1993-5117, November 1993.

Sakai, T. & Olejniczak, J. (2001). Navier-Stokes Computations for Arcjet Flows, AIAA Paper 2001-3014, June 2001.

Sakai, T. & Olejniczak, J. (2003). Improvement in a Navier-Stokes Code for Arc Heater Flows, AIAA Paper 2003-3782, June 2003.

Sakai, T. (2007). Computational Simulation of High-Enthalpy Arc Heater Flows, Journal of Thermophysics and Heat Transfer, Vol. 21, No. 1, 2007, 77-85.

Smith, R., Wagner, D. A., & Cunningham, J. W. (1996). Experiments with a Dual Electrode Plasma Arc Facility at the Deutsche Forschungsanstalt fur Luft-und Raumfahrt E.V. (DLR), AIAA Paper 96-2211, June 1996.

Terrazas-Salinas, I. & Cornelison, C. (1999). Test Planning Guide for ASF Facilities, A029-9701-XM3 Rev. B, March 1999.

Watson, V. R. & Pegot, E. B. (1967). Numerical Calculations for the Characteristics of a Gas Flowing Axially Through a Constrictor Arc, NASA TN D-4042, June 1967.

Wilcox, D. C. (1998). Turbulence Modeling for CFD, 2nd ed., DCW Industries, La Canada, CA, 1998, 119–122.

Whiting, E. E., Park, C., Liu, Y., Arnold, J. O., & Paterson, J. A. (1996). NEQAIR96, Non-equilibrium and Equilibrium Radiative Transport and Spectra Program: User Manual, NASA Reference Publication 1389, December 1996.

Yos, J. M. (1963). Transport Properties of Nitrogen, Hydrogen, Oxygen, and Air to 30,000 K, RAD-TM-63-7, March 1963.

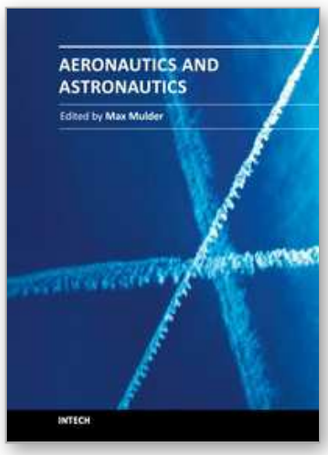


**Aeronautics and Astronautics**

Edited by Prof. Max Mulder

ISBN 978-953-307-473-3
Hard cover, 610 pages
**Publisher** InTech
**Published online** 12, September, 2011
**Published in print edition** September, 2011

In its first centennial, aerospace has matured from a pioneering activity to an indispensable enabler of our daily life activities. In the next twenty to thirty years, aerospace will face a tremendous challenge - the development of flying objects that do not depend on fossil fuels. The twenty-three chapters in this book capture some of the new technologies and methods that are currently being developed to enable sustainable air transport and space flight. It clearly illustrates the multi-disciplinary character of aerospace engineering, and the fact that the challenges of air transportation and space missions continue to call for the most innovative solutions and daring concepts.



**InTech Europe**
University Campus STeP Ri
Slavka Krautzeka 83/A
51000 Rijeka, Croatia
Phone: +385 (51) 770 447
Fax: +385 (51) 686 166
www.intechopen.com

**InTech China**
Unit 405, Office Block, Hotel Equatorial Shanghai
No.65, Yan An Road (West), Shanghai, 200040, China
中国上海市延安西路65号上海国际贵都大饭店办公楼405单元
Phone: +86-21-62489820
Fax: +86-21-62489821

IntechOpen